Electronic supplementary information for the paper:

Close-packing effect of water clusters within metal–organic framework pores on proton conductivity: a dielectric relaxation phenomenon in loose space and colossal dielectric permittivity

Bingtang Chen, [a] Fengxia Xie, [*a] Xiaoqiang Liang, [*a] Chengan Wan, [b] Feng Zhang, Lei Feng, [b] Qianmeng Lai, [a] Ziyan Wang, [a] and Chen Wen [*b]

[a] *College of Environmental and Chemical Engineering, Xi'an Polytechnic University, Xi'an 710048, PR China. E-mail: anxiny@163.com, xq-liang@163.com*
[b] *Beijing Spacecrafts Manufacturing Factory, Beijing 100094, PR China. E-mail: 13552907280@163.com*
[c] *Key Laboratory of Photochemical Biomaterials and Energy Storage Materials, Heilongjiang Province and College of Chemistry and Chemical Engineering, Harbin Normal University, Harbin 150025, PR China.*

Table of Contents

I. Crystallographic data and structures

Table S1 Crystallographic data and details of refinements for **Sm-fum-7H_2O** and **Er-fum-12H_2O**[1,2]

Compounds	**Sm-fum-7H_2O**	**Er-fum-12H_2O**
Empirical formula	$C_{12}H_{16}O_{19}Sm_2$	$C_6H_{15}O_{12}Er$
*M*r	764.97	446.44
Crystal system	Monoclinic	Monoclinic
Space group	$P2_1/n$	$P2_1/c$
a (Å)	9.5178(2)	8.457(1)
b (Å)	14.6999(3)	17.225(1)
c (Å)	14.8740(3)	9.690(1)
α (°)	90	90
β (°)	91.2425(9)	112.22(1)
γ (°)	90	90
V (Å^3)	2080.54(7)	1306.7(2)
Z	4	4
D_c (g cm^{-3})	2.442	2.269
μ(mm^{-1})	5.684	6.480
F(000)	1456	860
θ range [º]	3.5– 27.5	2.4– 25.0
Collected reflections	36935	2619
Unique reflections	4765	2289
Parameters	330	182
T (K)	180	293
R_1 [a], wR_2[b] [I > 2σ (I)]	0.0284, 0.0568	0.0314, 0.1159
GOF	0.93	1.18
Largest peak and hole (e ·Å^{-3})	-1.22, 1.28	-1.47, 0.94

[a] $R_1 = \sum||F_o|-|F_c||/\sum|F_o|$. [b] $wR_2 = [\sum w(|F_o^2|-|F_c^2|)^2/\sum w(|F_o^2|)^2]^{1/2}$

Table S2 Coordination Bond Lengths (Å) for **Sm-fum-7H_2O** and **Er-fum-12H_2O**.

Sm-fum-7H_2O			
Sm(1)−O(1)	2.628(3)	Sm(2)−O(1)	2.472(3)
Sm(1)−O(2)	2.509(3)	Sm(2)−O(5)	2.623(3)
Sm(1)−O(5)	2.416(3)	Sm(2)−O(6)	2.498(3)
Sm(1)−O(9)	2.352(3)	Sm(2)−O(10)	2.467(3)
Sm(1)−O(13)	2.449(3)	Sm(2)−O(15)	2.430(3)
Sm(1)−O(14)	2.407(3)	Sm(2)−O(16)	2.469(3)
Sm(1)−O(3a)	2.555(3)	Sm(2)−O(8c)	2.371(3)
Sm(1)−O(4a)	2.469(3)	Sm(2)−O(11d)	2.543(3)
Sm(1)−O(7b)	2.451(3)	Sm(2)−O(12d)	2.471(3)
Er-fum-H_2O			
Er(1)−O(1)	2.200(7)	Er(1)−O(5W)	2.431(7)
Er(1)−O(2)	2.341(6)	Er(1)−O(6)	2.392(6)
Er(1)−O(4)	2.320(7)	Er(1)−O(6W)	2.400(7)
Er(1)−O(5)	2.462(5)	Er(1)−O(3a)	2.254(6)

Symmetry codes: a) 1+*x*, *y*, *z*; b) 1/2+*x*, 1/2−*y*, 1/2+*z*; a) 1+*x*, *y*, *z*; b) −*x*, −*y*, 2−*z* for **Sm-fum-7H_2O**; a) *x*, 3/2−*y*, 1/2+*z* for **Er-fum-H_2O**.

Table S3 Hydrogen−bonding geometry parameters (Å, °) for **Sm-fum-7H_2O and Er-fum-12H_2O**

D−H···A	d(D−H)	d(H···A)	d(D···A)	∠(DHA)
	Sm-fum-7H_2O			
O(13) − H(131)···O(12)	0.93(4)	1.89(4)	2.781(4)	159(4)
O(13−H(132)···O(1)	0.95(4)	2.49(5)	2.808(4)	100(4)
O(13) −H(132)···O(17)	0.95(4)	1.94(4)	2.883(5)	174(4)
O(14) −H(141)···O(2)	0.93(5)	1.80(4)	2.734(4)	176(4)
O(14) −H(142)···O(6)	0.95(4)	1.82(4)	2.766(4)	172(4)
O(15) −H(151)···O(3)	0.97(3)	1.78(4)	2.739(4)	169(5)
O(15) − H(152)···O(17)	0.97(3)	1.84(3)	2.794(5)	167(5)
O(16) −H(161)···O(7)	0.93(4)	1.80(4)	2.694(4)	159(5)
O(16) − H(162)···O(4)	0.90(3)	2.02(3)	2.910(4)	170(5)
O(17) −H(171)···O(11)	0.95(4)	1.94(4)	2.887(5)	172(5)
O(17) −H(172)···O(18)	0.90(5)	2.19(5)	2.934(8)	139(4)
O(17) −H1(72)···O(19)	0.90(5)	2.00(5)	2.735(9)	138(4)
O(18)···O(19)	-	-	2.66	-
	Er-fum-12H_2O			
O(3W) −H(3WA)···O(6W)	1.0900	2.2000	3.058(12)	134.00
O(6W) −H(6WA)···O(1W)	0.8300	2.0200	2.766(10)	150.00
O(2W)−H(2WA)···O(1)	0.8300	2.5800	3.169(5)	129.00
O(3W)−H(3WB)···O(4WA)	1.1300	2.4600	3.035(14)	110.00
O(2W) −H(2WA)···O(2)	0.714(19)	2.48(9)	3.070(11)	142(11)
O(6W) −H(6WB)···O(4WA)	0.8700	2.5900	3.291(12)	138.00
O(6W) −H(6WB)···O(3W)	0.8700	2.3900	3.058(12)	134.00
O(4WA)−H(4WB)···O(1W)	0.9200	2.1000	2.940(12)	152.00
O(2W) −H(2WB)···O(3W)	1.1100	2.1400	2.843(13)	119.00
O(1W) −H(1WB)··· O(4)	1.1400	2.3700	3.149(10)	124.00
O(1W) −H(1WB)···O(6)	1.1400	2.4300	3.261(9)	128.00
O(5W)−H(5WB)···O(4WA)	0.9600	2.0300	2.902(13)	151.00

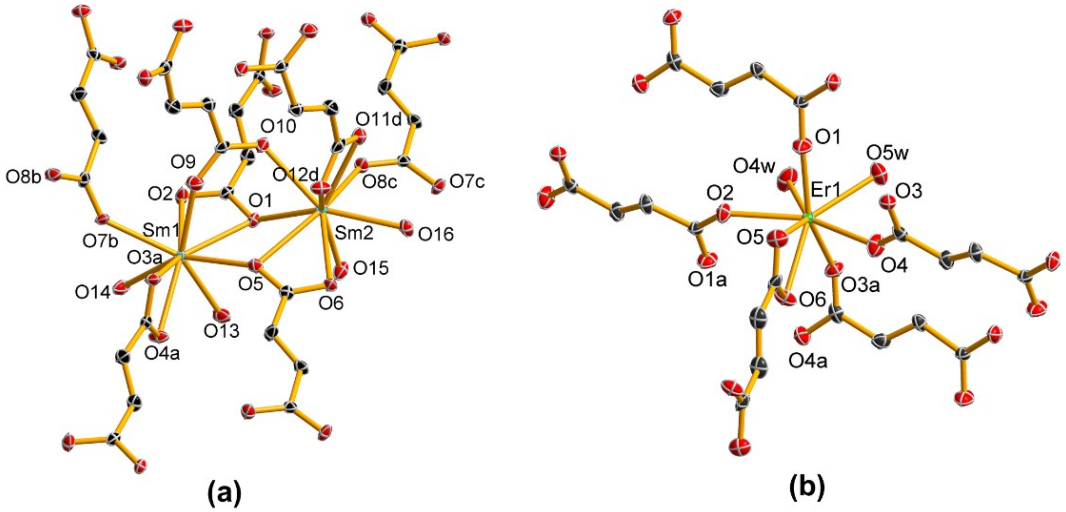

Fig. S1 (a) Coordination environment of Sm(III) in **Sm-fum-7H_2O**. Symmetry codes: a) 1+*x*, *y*, *z*; b) 1/2+*x*, 1/2−*y*, 1/2+*z*; c) 1+*x*, *y*, *z*; d) −*x*, −*y*, 2−*z*. (b) Coordination environment of Er(III) in **Er-fum-12H_2O**. Symmetry codes: a) *x*, 3/2−*y*, 1/2+*z*. Thermal ellipsoids are drawn at the 50% probability level. Hydrogen atoms have been omitted for clarity. (Colour code: black, C; red, O; cyan, Sm; green, Er).

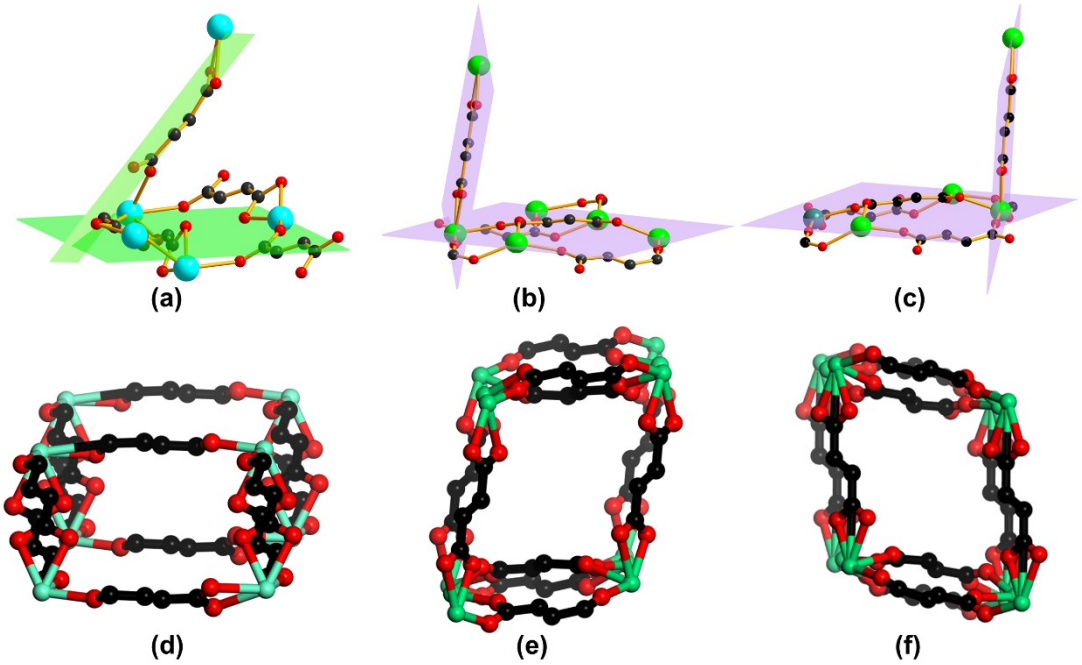

Fig. S2 Dihedral angles between the mean planes of the pillared fumarate ligands and the 2D layers formed by the fumarate ligands and lanthanide ions for **Sm-fum-7H_2O** (a), **Er-fum-12H_2O** (b) and **Er-fum-12H_2O** (c). The cavities or channels in **Sm-fum-7H_2O** (d), **Er-fum-12H_2O (e)** and **Er-fum-12H_2O** (f). Hydrogen atoms have been omitted for clarity. (Colour code: black, C; red, O; cyan, Sm; green, Er).

II. Characterization: PXRD patterns

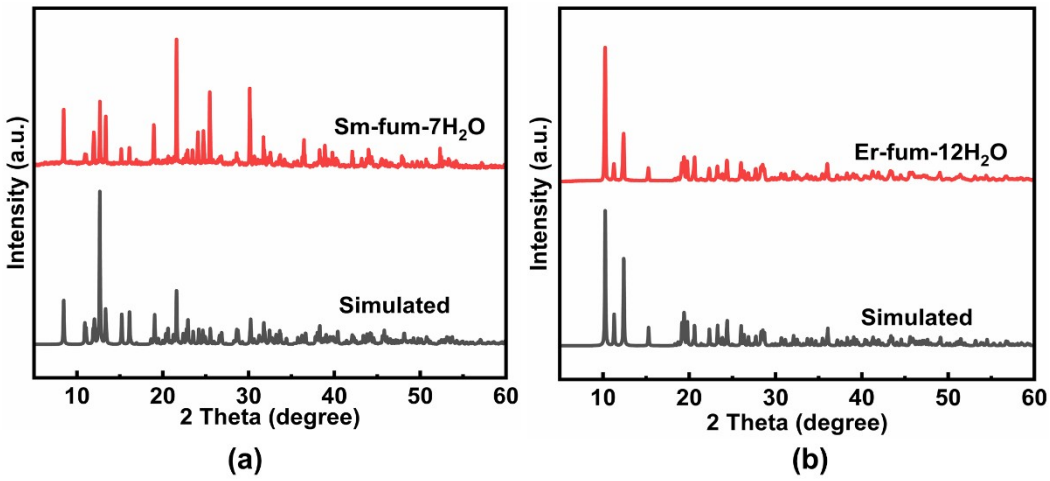

Fig. S3 The PXRD patterns for **Sm-fum-7H_2O** (a) and **Er-fum-12H_2O** (b) of a simulation based on single crystal data of reported and as-synthesized bulk crystals.

III. Characterization: IR spectra

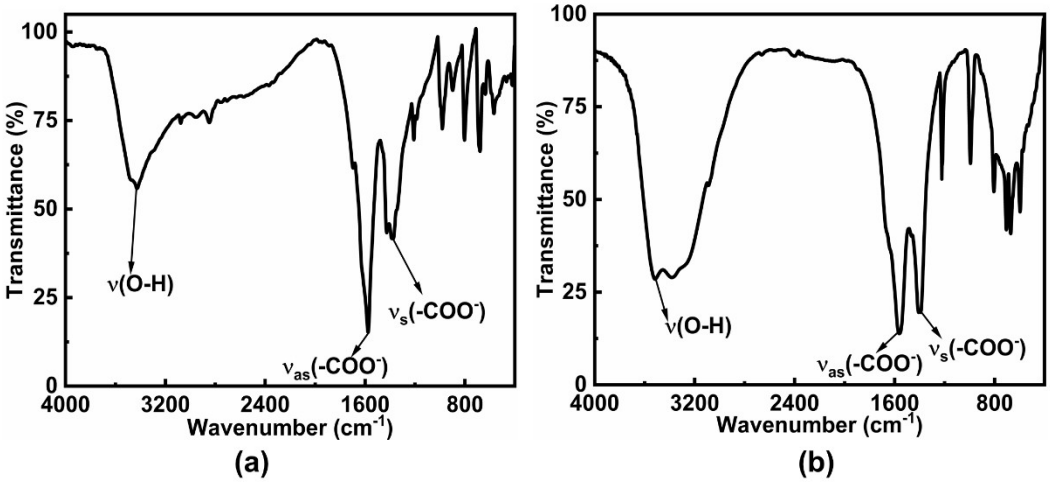

Fig. S4 IR absorption spectra of **Sm-fum-7H_2O** (a) and **Er-fum-12H_2O** (b).

IV. Characterization: Purity

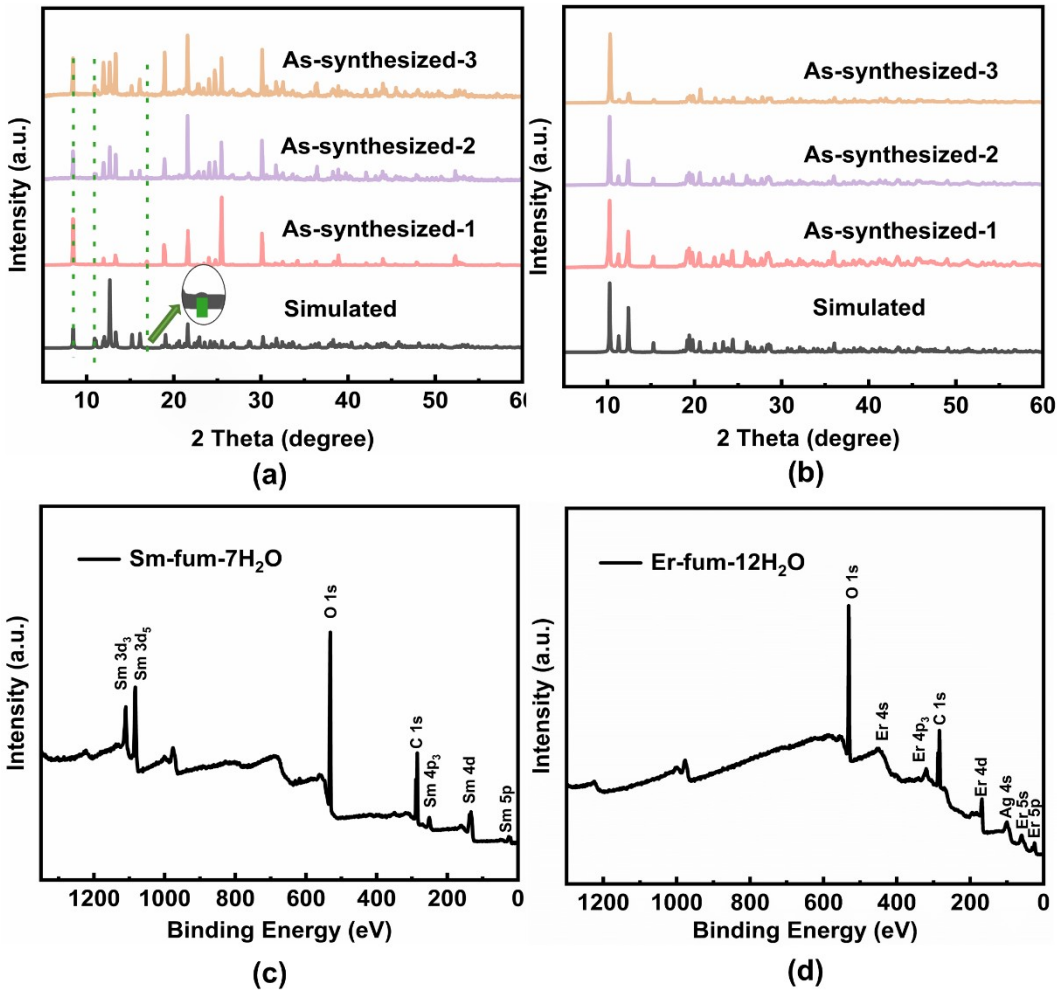

Fig. S5 The PXRD patterns for **Sm-fum-7H$_2$O** (a) and **Er-fum-12H$_2$O** (b) of a simulation based on single crystal data of reported and three as-synthesized bulk samples. The XPS survey spectra for **Sm-fum-7H$_2$O** (c) and **Er-fum-12H$_2$O** (d).

The influence of impurities or defects on the proton conductivity of MOFs is well-documented in the literature. For example, in 2015, S. Kitagawa's study demonstrated that manipulating ligand defects within UiO-66 could enhance proton conductivity by nearly three orders of magnitude, achieving a remarkable 6.93×10^{-3} S·cm^{-1} at 65 °C and 95% RH.[3] This finding emphasizes the potential of deliberately introducing ligand defects to control proton mobility and improve the proton-conducting properties of MOFs. Further research by H. Hou and his team in 2021 revealed that ligand exchange, which introduced pore defects within MOF crystals, significantly enhanced proton transfer. Their findings indicated that the proton conductivity of MOF-bpy reached 1.27×10^{-3} S·cm^{-1}, which is 3.5 times greater than that of MOF-azo, while MOF-bpe

exhibited a proton conductivity of 1.01×10^{-3} S·cm^{-1}, 2.8 times higher than MOF-azo.[4]

In addition to proton conductivity, impurities or defects also significantly affect dielectric properties. Research by N. F. Shi demonstrated that defects in the Co_3O_4/N-C structure led to lower dielectric loss values relative to the defect-free Co_3O_4/C, suggesting that the presence of defects can enhance dielectric performance.[5] Similarly, H. Xu's investigation into defects in MOF materials found that the removal of small molecules induced defects and functional groups that facilitated energy transfer from adjacent states to the Fermi level, promoting Debye dipole relaxation and resulting in high-performance microwave absorbers with improved dielectric properties.[6]

In light of these findings, we conducted an investigation into the impurities or defects present in Sm-fum-$7H_2O$ and Er-fum-$12H_2O$. To confirm the phase purity of the synthesized samples, PXRD measurements were performed three times prior to impedance testing. As shown in Fig. S5a and b, the PXRD peak positions of the synthesized samples closely matched with the simulated data obtained from single crystal analysis, confirming the absence of experimental randomness and establishing that both Sm-fum-$7H_2O$ and Er-fum-$12H_2O$ are of pure phase. Additionally, XPS was employed to assess the elemental composition of Sm-fum-$7H_2O$ and Er-fum-$12H_2O$. The survey spectra, depicted in Fig. S5c and d, revealed the presence of only C, O, and Sm elements in Sm-fum-$7H_2O$, while Er-fum-$12H_2O$ contained C, O, and Er, with the exception of a trace amount of Ag, by utilizing Advantage software for peak identification. It should be noted that the presence of the Ag element in the XPS measurement may be attributed to the adhered silver conductive colloid in the Er-fum-$12H_2O$ sample under experimental conditions. The surface of the Er-fum-$12H_2O$ sample is more susceptible to contact with the silver conductive colloid due to its smaller size compared to the Sm-fum-$7H_2O$ sample. The combined analysis of the PXRD patterns and XPS survey spectra provides strong evidence that both Sm-fum-$7H_2O$ and Er-fum-$12H_2O$ are of pure phases, indicating the absence of impurities in these samples. Consequently, the properties subsequently tested accurately reflect the intrinsic characteristics of pure-phase single crystals, remaining uninfluenced by impurities.

V. Characterization: SEM images

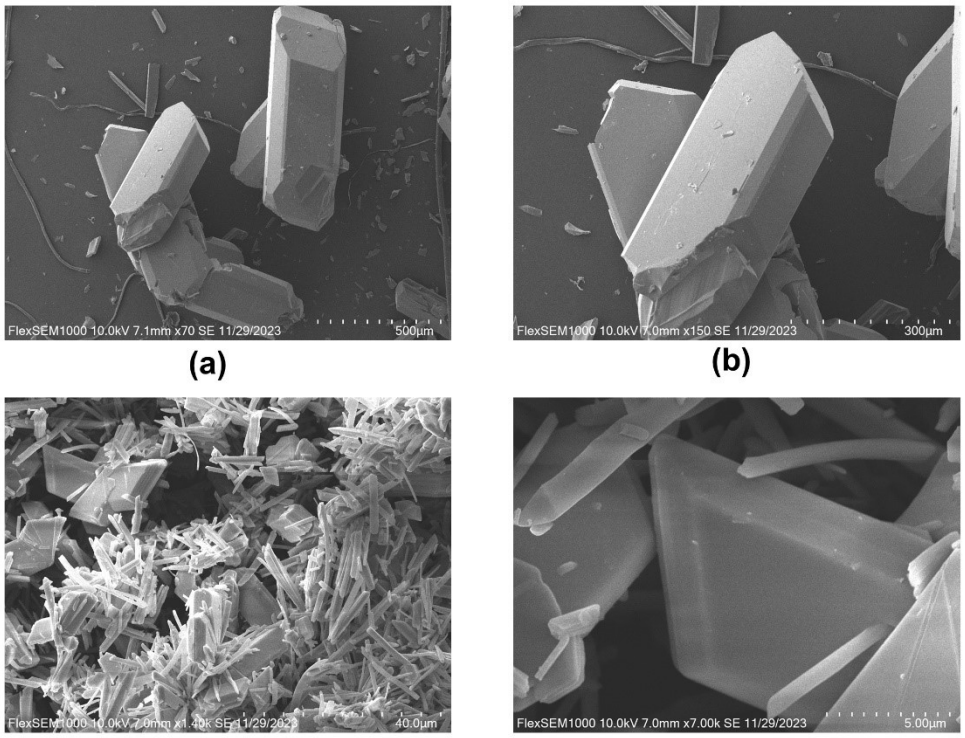

Fig. S6 SEM images of the full (a) and partial (b) views of **Sm-fum-H_2O** as well as the full (c) and partial (d) views of **Er-fum-12H_2O**.

VI. Characterization: Flexibility

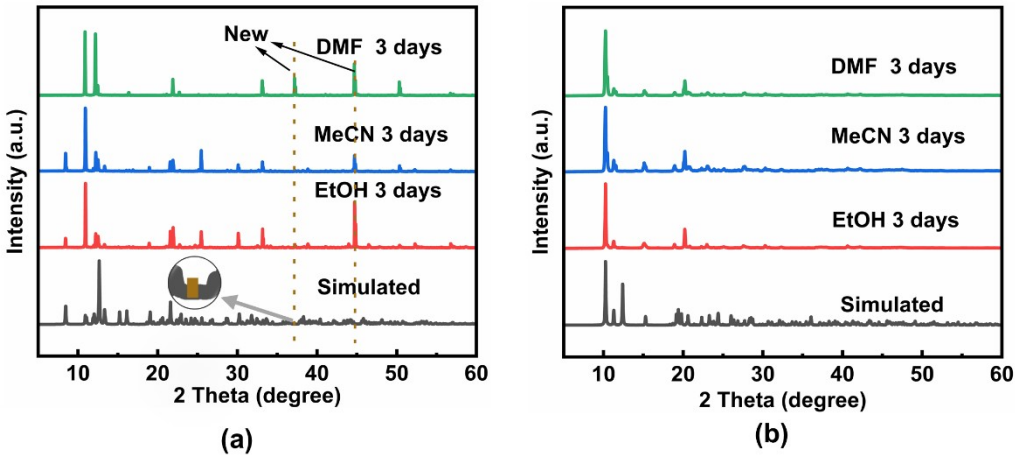

Fig. S7 Flexibility characterization. PXRD patterns of **Sm-fum-7H_2O** (a) and **Er-fum-12H_2O** (b) treated with EtOH, MeCN and DMF.

To assess the flexibility of the MOF frameworks, we conducted experiments involving immersion in organic solvents on Sm-fum-7H_2O and Er-fum-12H_2O. Specifically, Sm-fum-7H_2O and Er-fum-12H_2O were immersed in ethanol (10 ml), acetonitrile (10 ml), and DMF (10 ml) for three days, respectively. Subsequently, the samples were recycled and subjected to XRD analysis. An shown in Figure S7a, the majority of characteristic peaks of Sm-fum-7H_2O remained intact and some new peaks were observed at 37.17° and 44.78°, indicating that a slight deformation of the framework. In other words, Sm-fum-7H_2O has a certain degree of flexibility, which is possibly associated with water molecules within the framework exchanging with the organic solvents. In contrast, no new peaks were observed in the XRD pattern of Er-fum-12H_2O (Figure S7b), indicating a lack of flexibility and a higher degree of structural rigidity compared to Sm-fum-7H_2O. However, the water-assisted proton conductivity measurements for these MOFs were carried out under ~97% RH condition, rather than in organic solvents. Besides, the PXRD patterns of Sm-fum-7H_2O and Er-fum-12H_2O almost remain unchanged following exposure to moisture, water, aqueous acidic and alkaline solutions. This indicates a good retention of their framework integrity, reflecting the inherent rigidity of these MOFs. Consequently, it can be concluded that the structural rigidity of these compounds remains largely unaffected under the tested conditions.

Furthermore, the potential changes in the arrangement of water clusters under the

measured conditions require a detailed single-crystal structure analysis for clarification. Unfortunately, suitable single crystals of Sm-fum-7H_2O and Er-fum-12H_2O are not available for such structural investigations, leaving the specific alterations in the arrangement of water clusters within the crystals unclear. However, a significant finding is that a good linear relationship was observed within the measured temperature range for both Sm-fum-7H_2O and Er-fum-12H_2O. The analysis yielded activation energies of 0.12 eV for Sm-fum-7H_2O and 0.27 eV for Er-fum-12H_2O. The fact that single values were determined for each MOF, rather than a range of values, implies a uniformity in the mechanisms. In other words, the arrangement of water clusters remains largely unchanged within the measured temperature range, providing some insight into the stability of the water cluster configuration in these MOFs.

The flexibility and rigidity of MOFs are indeed critical factors that significantly influence their proton-conducting properties. As demonstrated in previous studies, such as the investigation of the flexible MOF BUT-8(Cr)A, an increase in RH leads to a greater adsorption of water molecules within the framework.[7] The increase in water content enhances the number of available proton carriers and can establish more effective hydrogen bonding networks with the oxygen and nitrogen atoms in the organic ligands. The result facilitates the transportation of protons, highlighting the importance of MOF flexibility in enhancing proton conductivity under humid conditions. Further research by S. Kitagawa on the MOF material TJU-102 revealed exceptional proton conductivity attributed to its structural characteristics. The high density of free carboxyl (−COOH) groups within the pores of TJU-102 allows the framework to transition from a state of high rigidity to one of low flexibility, which is accompanied by tailored porosity. This unique combination of two properties results in remarkable proton conductivity, achieving values as high as 5.26 $\times 10^{-2}$ S cm^{-1} at 363 K with 98% RH.[8] These findings revealed that the structural flexibility plays in optimizing the proton-conducting capabilities of MOFs, making them promising candidates for applications in fuel cells and other energy-related technologies.

VII. Stability: TGA curves

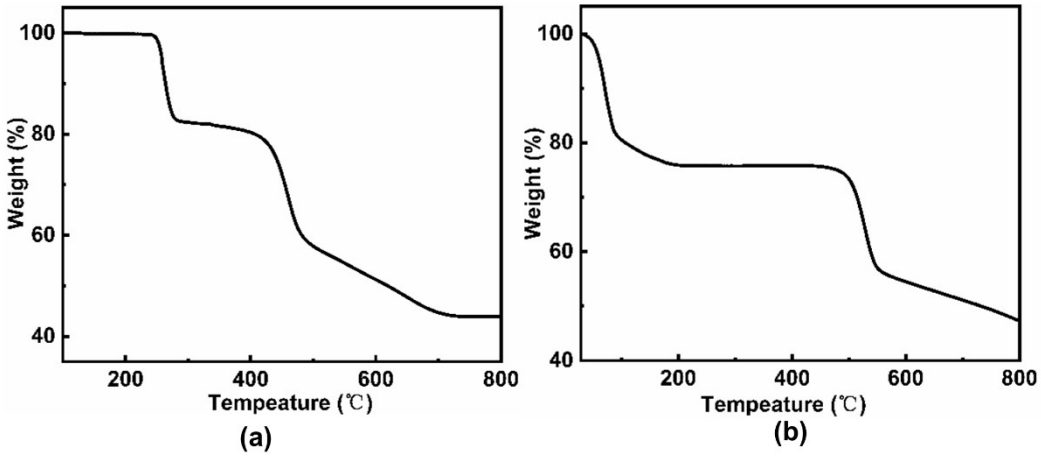

Fig. S8 Thermogravimetric curves for **Sm-fum-H_2O** (a) and **Er-fum-12H_2O** (b).

VIII. Hydrophilicity: water adsorption and water contact angle

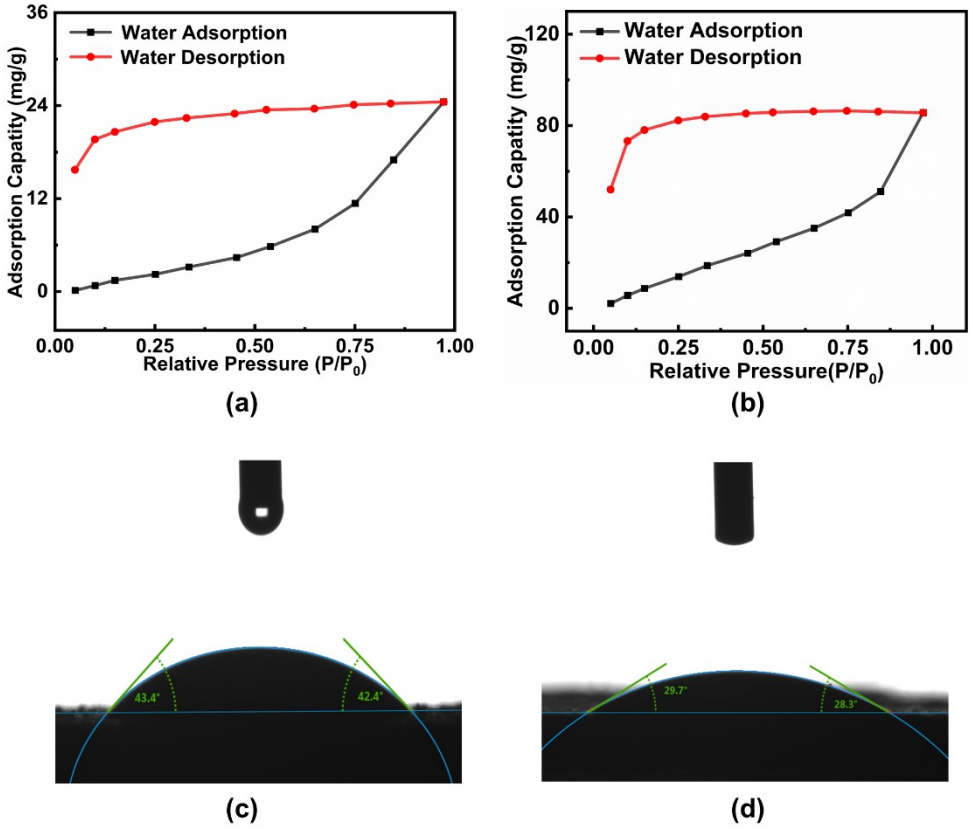

Fig. S9 Water adsorption–desorption isotherms of **Sm-fum-7H_2O** (a) and **Er-fum-12H_2O** (b) at 298 K. Water contact angles of **Sm-fum-7H_2O** (c) and **Er-fum-12H_2O** (d) at 298 K.

IX. Electrochemical measurements: impedance spectra

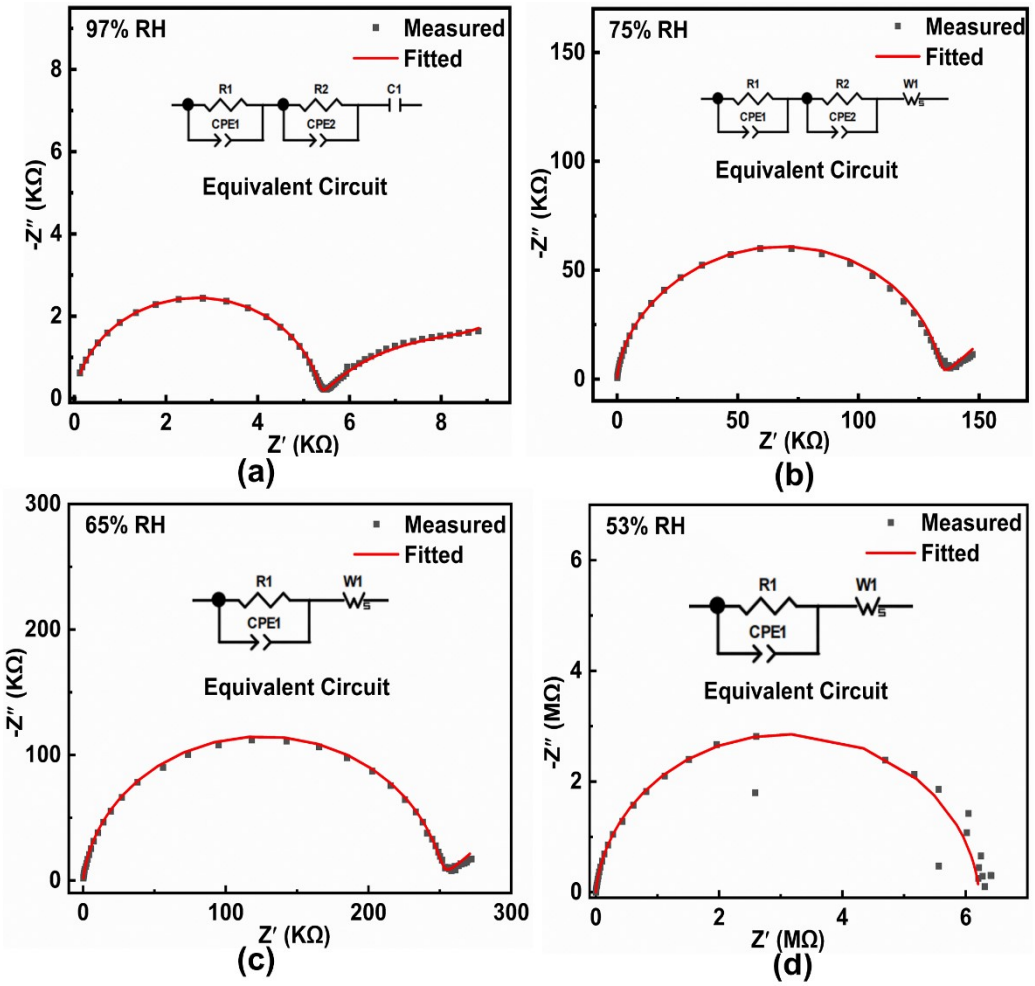

Fig. S10 Nyquist plots of **Sm-fum-H_2O** under 97% (a), 75% (b), 65% (c), and 53% (d) RHs (relative humidities) at 298 K (R1, bulk resistor; R2, grain boundary resistor; CPE, constant phase element; W1, Warburg diffusion element).

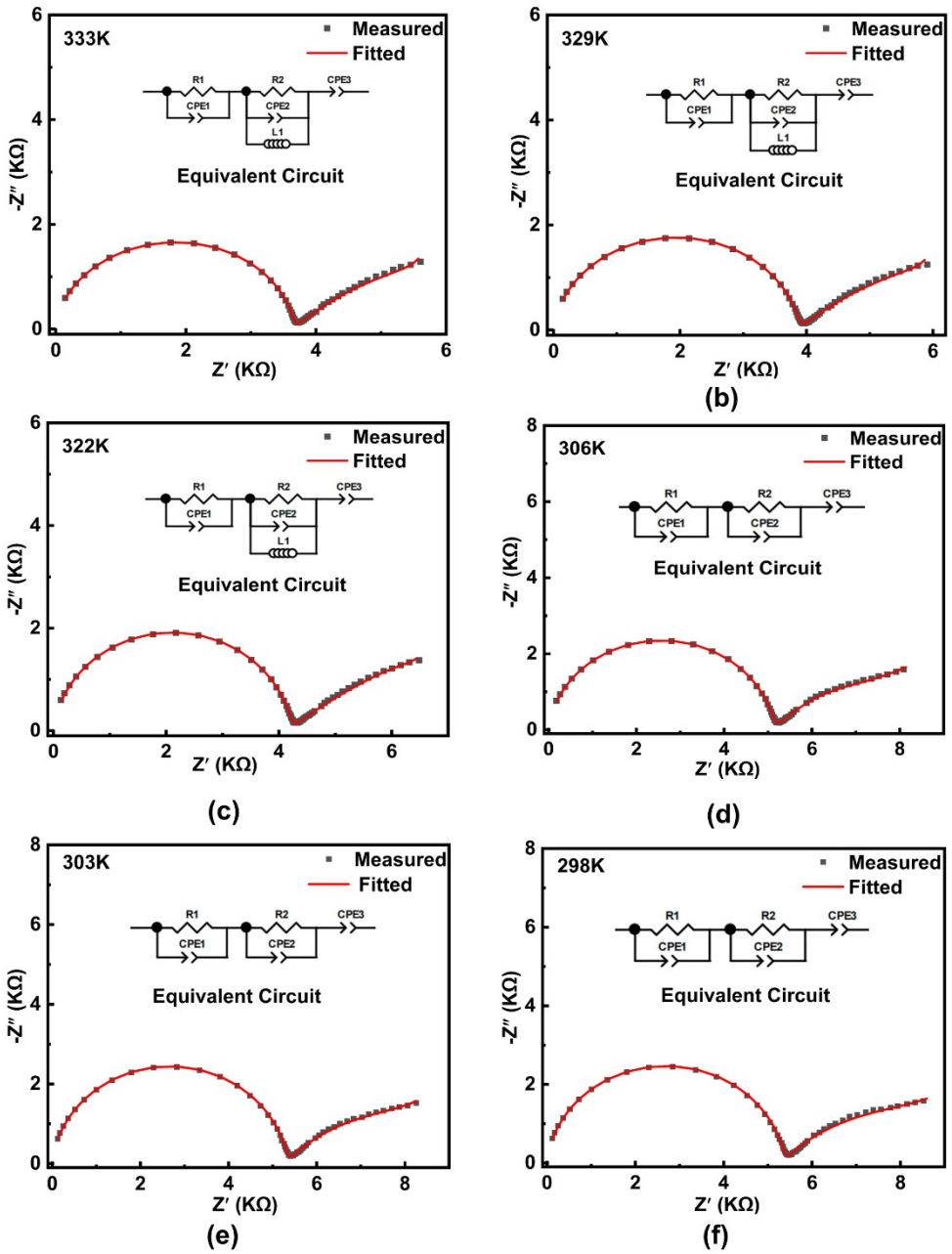

Fig. S11 Nyquist plots of **Sm-fum-H_2O** at 333 K (a), 329 K (b), 322 K (c), 306 K (d), 303 K (e) and 298 K (f) under ~97% RH (R1, bulk resistor; R2, grain boundary resistor; CPE, constant phase element; L1, inductor).

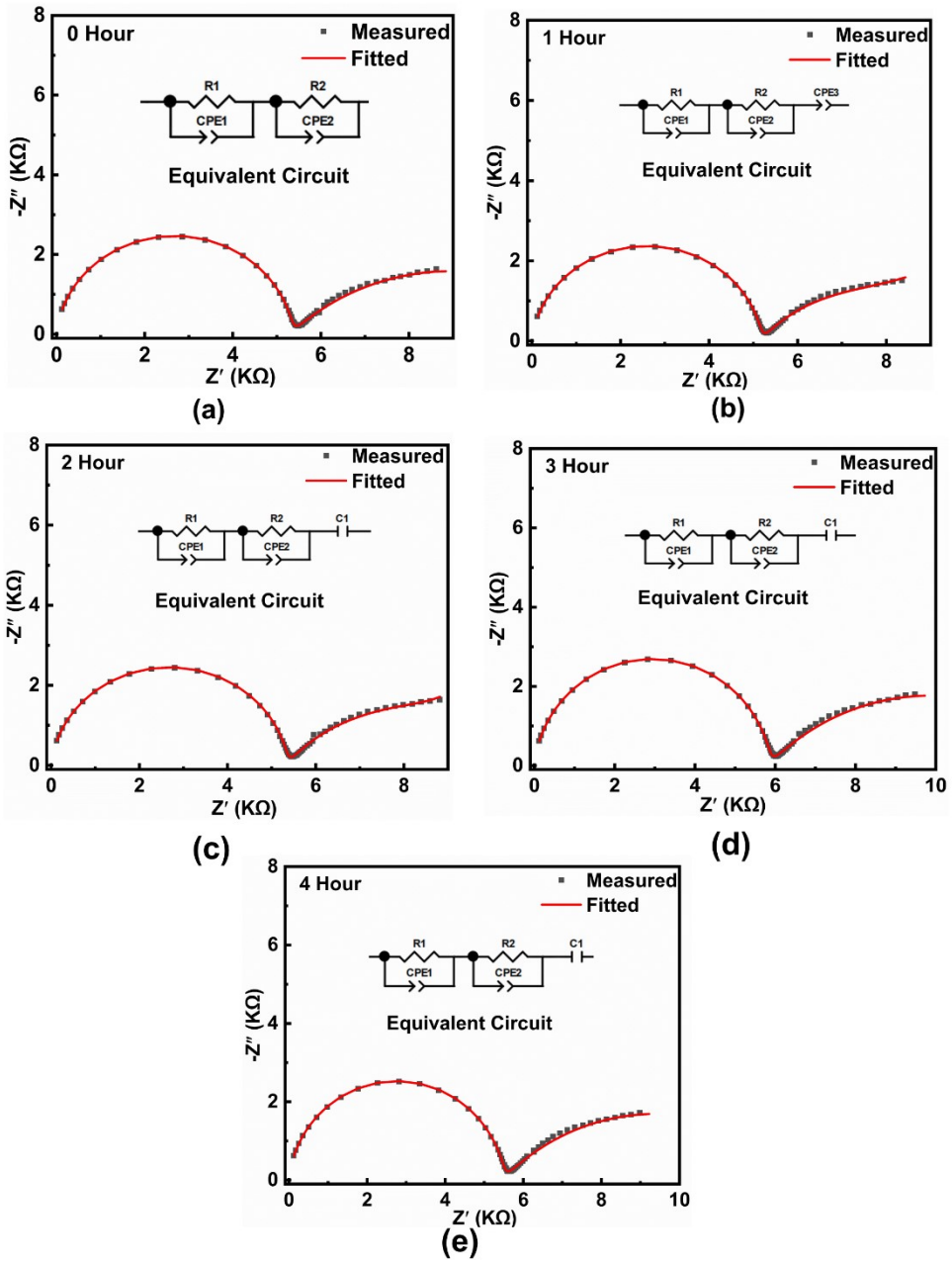

Fig. S12 Nyquist plots of **Sm-fum-H_2O** at 0 h (a), 1 h (b), 2 h (c), 3 h (d) and 4 h (f) under 298 K and ~97% RH conditions (R1, bulk resistor; R2, grain boundary resistor; CPE, constant phase element).

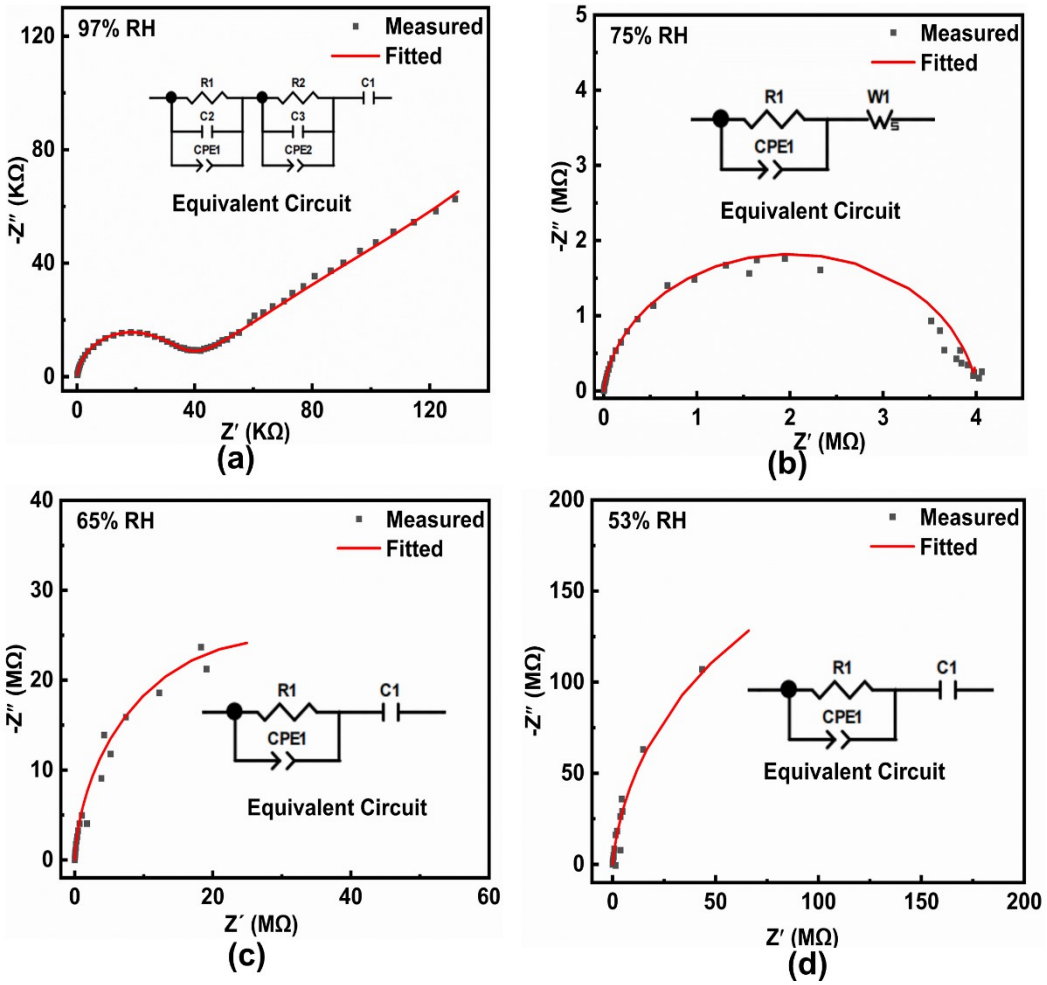

Fig. S13 Nyquist plots of **Er-fum-12H_2O** under ~97% (a), ~75% (b), ~65% (c) and ~53% (d) RHs at 298 K (R1, bulk resistor; R2, grain boundary resistor; CPE, constant phase element; W1, Warburg diffusion element).

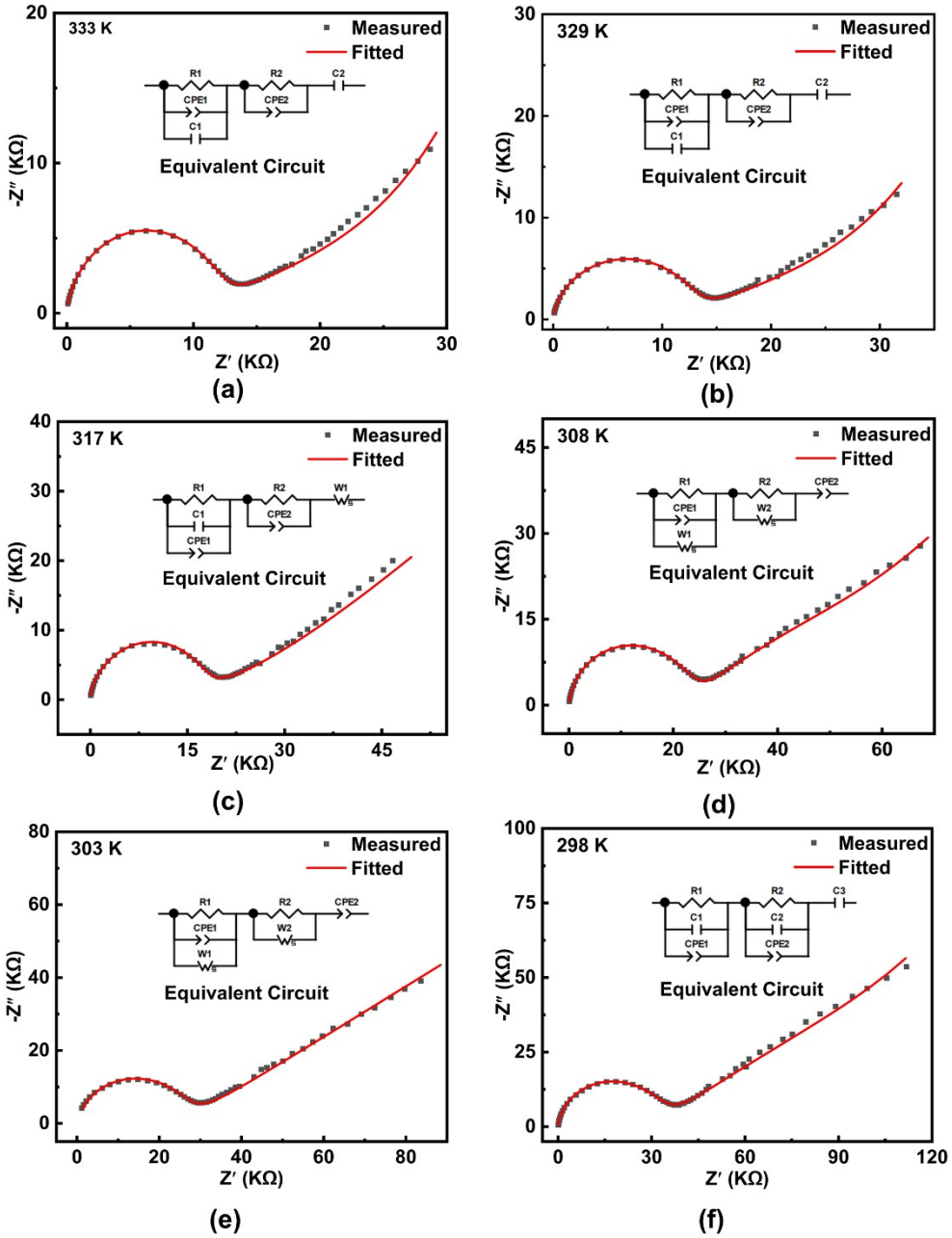

Fig. S14 Nyquist plots of **Sm-fum-H_2O** at 333 K (a), 329 K (b), 322 K (c), 306 K (d), 303 K (e) and 298 K (f) under ~97% RH (R1, bulk resistor; R2, grain boundary resistor; CPE, constant phase element; W1 and W2, Warburg diffusion element; L1, inductor).

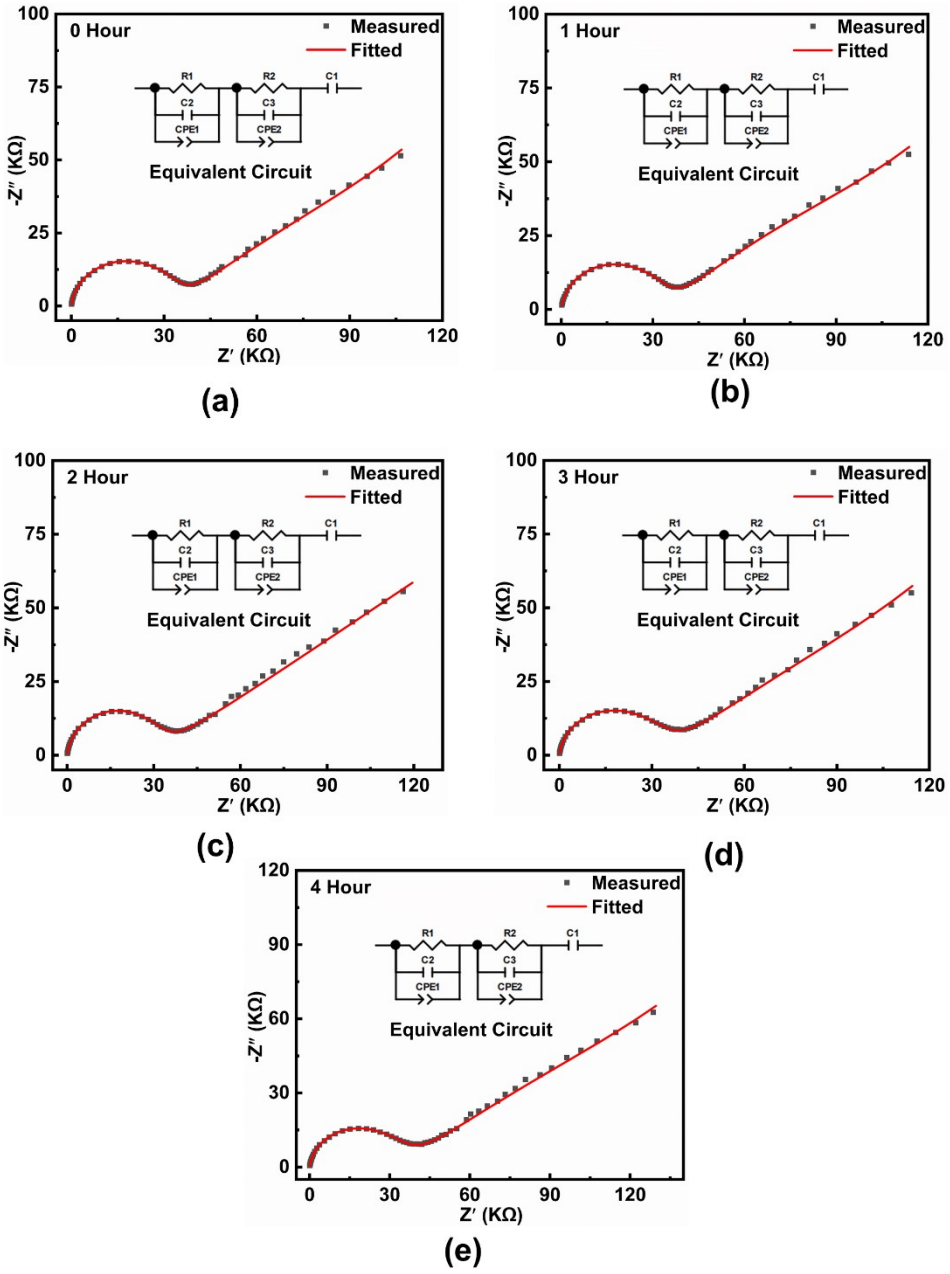

Fig. S15 Nyquist plots of **Er-fum-12H$_2$O** at 0 h (a), 1 h (b), 2 h (c), 3 h (d) and 4 h (f) under 298 K and ~97% RH conditions (R1, bulk resistor; R2, grain boundary resistor; CPE, constant phase element).

X. PXRD patterns after impedance measurements.

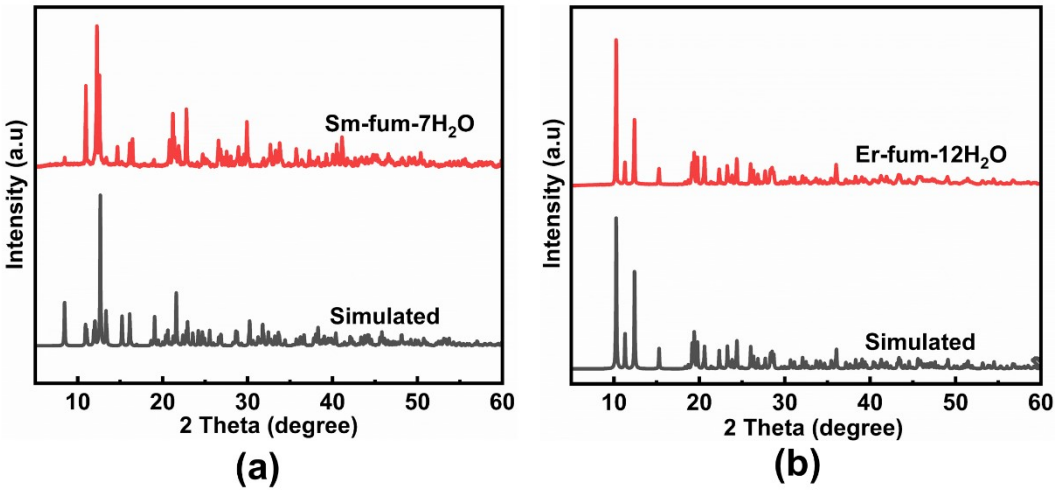

Fig. S16 PXRD patterns of simulations based on single-crystal analysis and after the impedance measurements for **Sm-fum-7H_2O** (a) and **Er-fum-H_2O** (b).

XI. DC conductivity and activation energy

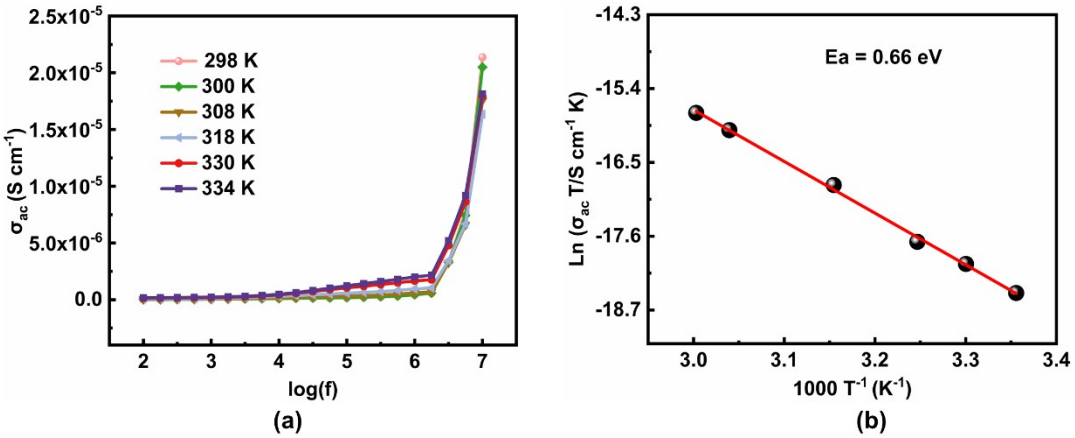

Fig. S17 Frequency dependence of the DC conductivity at different temperatures from 10^2 to 10^7 Hz for Er-fum-12H_2O (a) and activation energy (b).

XII. Differential scanning calorimeter measurements

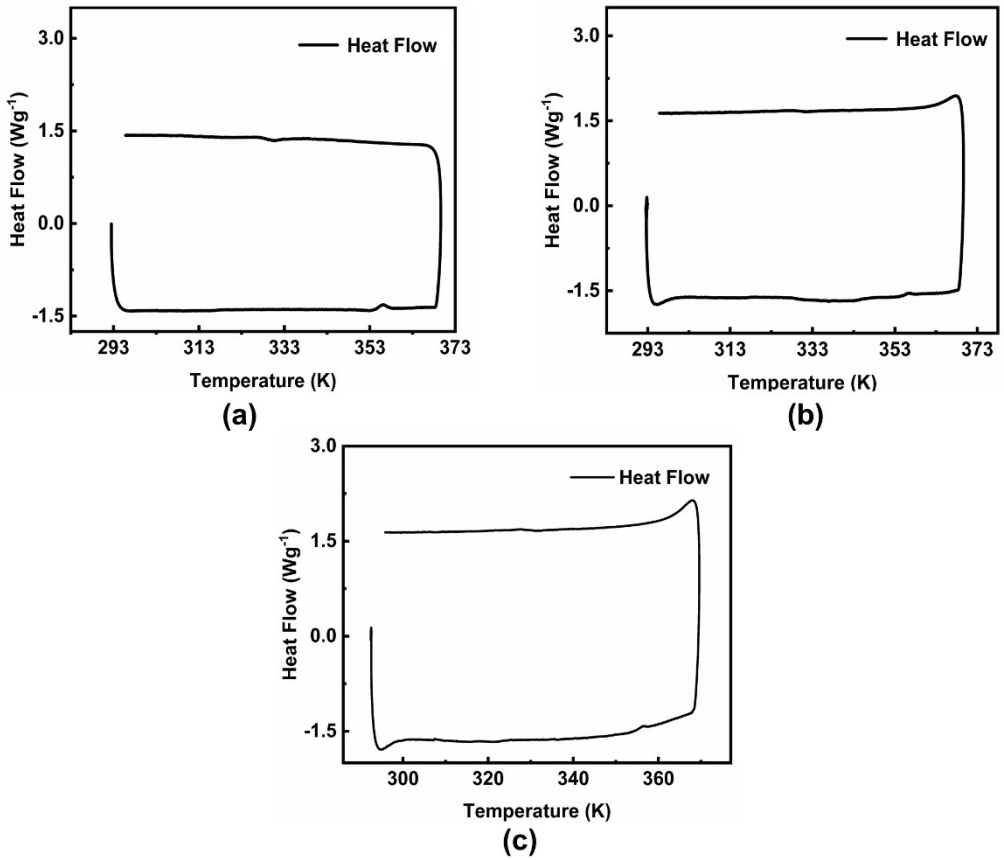

Fig. S18 DSC (Differential Scanning Calorimeter) curves of **Sm-fum-7H_2O** (a), **Er-fum-12H_2O** (b) and **blank sample** (c).

XIII. Dielectric spectrum

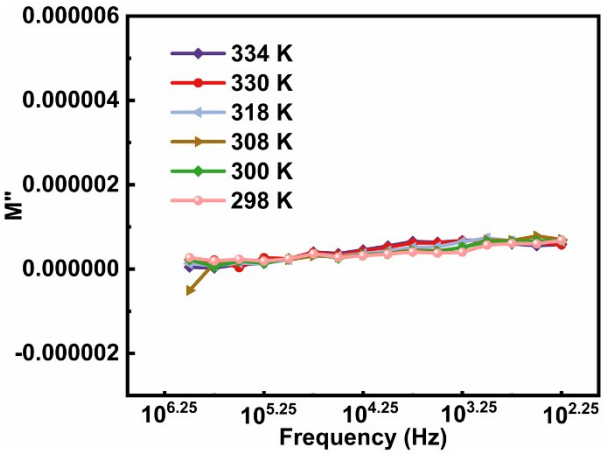

Fig. S19 Frequency dependence of the imaginary part of electric modulus at different temperatures from $10^{2.25}$ to $10^{6.25}$ Hz for **Sm-fum-7H_2O.**

XIV. Comparison of chemical stability

Table S4 Comparison of chemical stability of **Sm-fum-7H_2O** and **Er-fum-12H_2O** with reported MOF materials

Materials	pH range	Time (day or hour)	References
Sm-fum-7H_2O	2–12	24 hours	This work
Er-fum-12H_2O	2–12	3 days	This work
Cd-EDDA [a]	2–12	24 hours	9
COF-PDAN-AO	1–13	6 hours	10
BUT-155 [b]	4–10	24 hours	11
oCB-MOF-1 [c]	2–12	15 hours	12
PCN-600(Fe)	2–11	24 hours	13
PCN-250(Fe_2Co)	1–12	24 hours	14
PCN-777	3–11	12 hours	15
$[Cd_2(L1)(1,4\text{-}NDC)_2]_n$ [d]	3–13	48 hours	16
$[Cd(L_2)(1,4\text{-}NDC)]_n$ [e]	3–13	48 hours	16
Eu-MOF [f]	3–11	48 hours	17

[a] H_4EDDA = 5,5′-(ethane-1,2-diylbis(oxy))diisophthalic acid.[b] BUT = [Cu_4(tdhb)], H_8tdhb = 3,3′,5,5′-tetra(3,5-dicarboxyphenyl)-2,2′,4,4′,6,6′-hexamethylbiphenyl). [c] oCB-MOF-1 = [$Zn_4(\mu_4\text{-}bdc)_2(\mu_2\text{-}oCB\text{-}L)_2(\mu_3\text{-}O)_2\text{-}(DMF)_2]\cdot 4DMF$, H_2bdc = 1,4-benzenedicarboxylate, oCB-L = 1,2-bis{(pyridin-3- yl)methanol}-1,2-dicarba-closo-dodecarborane .[d] L_1 = 1,4-bis(benzimidazol-1-yl)-2-butylene, 1,4-H_2NDC = 1,4-naphthalenedicarboxylic acid .[e] L_2 = 1,4-bis(2-methylbenzimidazol-1-yl)-2-butylene .[f] Eu-MOF = $[Me_2NH_2]_2(Eu)_2(ofdp)_2(DMF)(H_2O)]\cdot 7H_2O\cdot DMF$, H_4ofdp = 5,5′-(9-oxo-9*H*-fluorene-2,7-diyl)diisophthalic acid.

XV. Comparison of proton conductivity

Table S5 Comparison of proton conductivity of **Sm-fum-7H_2O** and **Er-fum-12H_2O** with some reported proton conductors

Materials	σ (S cm^{-1})	*Ea* (eV)	*T* (K)	*RH* *(%)*	Reference
Sm-fum-7H_2O	6.9×10^{-4}	0.12	333	97	This work
Er-fum-12H_2O	1.6×10^{-4}	0.27	333	97	This work
$[Ni_2(dobdc)(H_2O)_2]\cdot6H_2O$[a]	1.4×10^{-4}	0.12	353	95	18
$Ni_2(dobdc)$	1.4×10^{-4}	-	353	95	18
Zn-pzdc-H_3O^+[b]	2.42×10^{-3}	0.21	323	97	19
Mn-pzdc-H_3O^+	2.03×10^{-3}	0.10	323	97	19
Cu-Hpzdc-H_2O	1.68×10^{-3}	0.35	323	97	19
Co-2PPA[c]	2.96×10^{-4}	0.29	333	97	20
Co-4PPA	2.78×10^{-5}	0.31	333	97	20
$Zr(L)_2X_2H_2\cdot5H_2O$[d]	1×10^{-4}	0.23	353	95	21
$\{[Gd(ma)(ox)(H_2O)]_n\cdot3H_2O\}$ [e]	4.7×10^{-4}	0.88	353	95	22
$\{[Dy(ma)(ox)(H_2O)]_n\cdot1.5H_2O\}$	9.06×10^{-5}	0.70	353	95	22
MOF-808-OX	4.25×10^{-4}	0.14	353	98	23
$[Mg(2,2',6,6'\text{-BPTC})_{0.5}(H_2O)_3]\cdot5H_2O$ [f]	2.6×10^{-4}	0.47	373	98	24
Fe-MOF	1.25×10^{-4}	0.385	333	98	25
$[Cu_4(HDMPhIDC)_4(H_2O)_4]_n$[g]	1.3×10^{-4}	0.95	373	98	26
$\{[Cd(p\text{-}TIPhH_2IDC)_2]\cdot H_2O\}_n$[h]	1.24×10^{-4}	0.32	373	98	27
$[Cu(bpdc)(H_2O)_2]_n$[i]	1.55×10^{-4}	-	373	98	28
$\{[Co(BPTA)(BDA)](DMF)\cdot1.3H_2O\}_n$ [j]	9.5×10^{-4}	-	353	98	29
$\{[Co(BPTA)(OBA)](2DMF)\cdot6H_2O\}_n$ [k]	6.6×10^{-4}	-	353	98	30
$[(CuI\quad 4CuII\ 4NTAA_4)\cdot3H_2O]_n$	4.9×10^{-4}	0.39	373	98	30
UiO-66-AS	1.7×10^{-4}	-	353	98	31
$\{[Co_3(p\text{-}ClPhHIDC)_3(H_2O)_3]\cdot6H_2O\}_n$ [l]	2.47×10^{-4}	0.20	363	93	32
$\{[Co_3(m\text{-}BrPhIDC)_2(H_2O)_6]\cdot2H_2O\}_n$	7.64×10^{-4}	0.56	373	98	32
$[Zn(o\text{-}BrPhH_2IDC)_2(H_2O)_2]\cdot EtOH\cdot3H_2O$ [m]	1.14×10^{-4}	0.72	373	98	33
$[Co(o\text{-}BrPhH_2IDC)_2(H_2O)_2]\cdot EtOH\cdot3H_2O$	3.11×10^{-4}	0.89	373	98	33
$[\{(H_3O)[Eu(SBDB)(H_2O)_2]\}$	1.0×10^{-4}	0.48	338	98	34

JXNU-7(Eu)[n]	1.04×10^{-4}	0.34	358	98	35
Tb-DSOA	1.66×10^{-4}	0.45	373	98	36
CuH(Hspip)(HPO_4) H_2O[o]	6.90×10^{-4}	0.68	368	97	37
UMOM-100-b	2.11×10^{-4}	0.66	353	90	38
[Pr(betc)(H_2O)$_2$] (H_2pip)$_{0.5}$}$_n$[p]	8.9×10^{-5}	0.33	313	97	39
PPA	2.49×10^{-5}	0.27	325	97	40
[Cu(PPA)I]	1.64×10^{-4}	0.19	325	97	40
[Co(PPA)$_2$(BDC)(H_2O)$_2$·(PPA)$_2$ (H_2BDC)$_2$(H_2O)][q]	2.29×10^{-4}	0.24	325	97	40
JUC-125[r]	1.5×10^{-4}	0.32	323	97	41
{[Pr_2Ca(betc)$_2$(H_2O)$_7$]· H_2O}$_n$	3.2×10^{-5}	0.66	305	97	42
OCC 2[s]	3.72×10^{-4}	0.21	299	97	43
LOF 1[t]	9.3×10^{-5}	0.33	303	97	44
PMOCP 3[u]	1.38×10^{-4}	0.14	323	97	45
Co-ppca-2D [v]	3.21×10^{-5}	0.193	333	97	46

Note: σ = proton conductivity (S cm^{-1}). E_a = activation energy (eV). T = temperature (K). RH = relative humidity (%). [a] dobdc = 2,5-dioxido-1,4-benzenedicarboxylate. [b] H_2pzdc = 2,3-pyrazinedicar-boxylic acid. [c] PPA = 4-(3-pyridinyl)-2-amino pyrimidine. [d] L = $(O_3PCH_2)_2N$-C_6H_{10}-$N(O_3CH_2P)_2$, X = H, Na^+, NH_4^+. [e] H_2L = mucic acid, H_2Ox = oxalic acid. [f] BPTC = 2,2′,6,6′-tetracarboxybiphenyl. [g] HDMPhIDC = 2-(3,4-dimethyl)phenyl-4,5-imidazole dicarboxylic acid. [h] p-TIPhH_2IDC = 2-p-(1*H*-1,2,4-triazolyl)phenyl-1*H*-4,5-imidazoledicarboxylic acid. [i] H_2bpdc = 2,2′-bipyridyl-3,3′-dicarboxylic acid. [j] BDA=benzene-1,3-diacrylicacid. [k] OBA = dicarboxylates 4,4'-oxybisbenzoic acid. [l] p-ClPhH_3IDC = 2-(p-chlorophenyl)-imidazole-4,5-dicarboxylicacid. [m] o-BrPhH_2IDC = 2-(o-bromo) phenyl-4, 5-imidazole dicarboxylic acid. [n] XNU-7= {[Ln_3(μ_2-OH)(DSNPDC)$_2$(H_2O)$_x$]·yH_2O}$_n$, H_4-DSNPDC= 5,7-disulfonate-1,4-naphthalenedicarboxylic acid. [o] Hspip= 2-sulfophenylimidazo(4,5-f)(1,10)-phenanthroline. [p] H_4betc = 1,2,4,5-benzenetetra- carboxylic acid, pip = piperazine. [q] H_2BDC = 1,4-benzenedicarboxylic acid. [r] JUC-125 = {[Gd_4(R-ttpc)$_2$(R-Httpc)$_2$($HCOO$)$_2$(H_2O)$_8$]·4H_2O}$_n$, R-H_3ttpc = (3R,3′R,3″R)-1,1′,1″-(1,3,5-triazine-2,4,6-triyl)-tripiperidine-3-carboxylic acid. [s] OCC2 = (H_3betc)$_2$(H_2-Mepip)·(H_2O), Hopip = homopiperazine. [t] LOF 1 = {[Er_3(pmpc)(C_2O_4)$_3$(H_2O)$_7$]·2H_2O}$_n$, D-H_3pmpc = D-1-(phosphono-methyl)piperidine-3- carboxylic acid. [u] PMOCP3 = {Cd(D-pmpcH)(H_2O)$_2$$Cl_2$}$_n$, D-$H_3$pmpc = 1-(phosphonomethyl)piperidine-3- carboxylic-acid. [v] H_2ppca = 5-(pyridin-3-yl)-1H-pyrazole-3-carboxylic acid)

XVI. Fitting of Cole-Cole plots

Table S6 M_0, M_∞ and α parameters obtained from the best fits for **Er-fum-12H$_2$O**.

T / K	M_0	M_∞	α	R^2
298 K	0.00661	2.18×10^{-4}	0.607	0.967
306 K	0.00672	2.14×10^{-4}	0.592	0.966
320 K	0.00729	2.10×10^{-4}	0.576	0.956
330 K	0.00741	1.96×10^{-4}	0.571	0.954
334 K	0.00756	1.80×10^{-4}	0.566	0.951

XVII. Comparison of dielectric constant

Table S7 Comparison of dielectric constant of **Sm-fum-7H_2O** and **Er-fum-12H_2O** with some reported proton conductors

Materials	Dielectric constant	Frequency (Hz)	Reference
Sm-fum-7H_2O	2.22 ×10^3	$10^{2.5}$	This work
Er-fum-12H_2O	4.95×10^5	10^2	This work
	1.42 ×10^5	$10^{2.5}$	This work
Co-2PPA[a]	620	10^2	21
Co-4PPA	630	10^2	21
(CBQ)CuI 3$(CN)_3$Br [b]	119.3	-	47
[(CBQ)CuI 3$(CN)_3$Br]$_n$	1.8 ×10^6	10^2	47
[Sm_2(bhc)(H_2O)$_6$]n [c]	45.1	5×10^3	48
[Mn_3($HCOO$)$_6$])(C_2H_5OH)	45	-	49
Co_2(1,4-bdc)$_2$(dabco)·[4DMF·1H_2O] [d]	5 ×10^3	10^2	50
Na[In_3(odpt)$_2$(OH)$_2$(H_2O)$_2$](H_2O)$_4$[e]	40.5	10^3	51
Cu:PI-Bpy (1:2)[g]	133	10^2	52
(EMI)$_2$[Zn_3(1,2,4,5-BTC)$_2$]·2H_2O}$_n$ [h]	5.6 ×10^6	10^2	53
$CaCu_3Ti_4O_{12}$	10^5	20	54
[CdCl(TBP)]$_n$[i]	1.2 ×10^7	10^2	55
$MAPbBr_3$	25.5	-	56
HNi-MOF-74-DMSO[j]	47	-	57

[a] PPA = 4-(3-pyridinyl)-2-amino pyrimidine. [b] CBQ-Br = N-4-cyanobenzyl quinidinium. [c] H_6bhc = benzenehexacarboxylic acid. [d] 1,4-bdc = 1,4-benzenedicarboxylate anions, dabco = 1,4-diazabicyclo [2.2.2] octane. [e] odpt = 4,4′-oxydiphthalate. [f] btc = 1,2,3-benzenetricarboxylate. [g] Bpy = (5,5′-bis[(4-amino)phenoxy]-2,2′-bipyrimidine). [h] [EMI]Br = 1-ethyl-3-methyl imidazolium bromide, 1,2,4,5-BTC = 1,2,4,5-benzenetetracarboxylate. [i] H-TBP = N-(4-(1H-tetrazol-5-yl)benzyl)proline. [j] DMSO = Dimethyl sulfoxide.

XVIII. Comparison of dielectric constant and proton conductivity

Table S8 The comparison of the proton conductivity and dielectric functions of **Sm fum-7H_2O** and **Er-fum-12H_2O**.

Materials	Proton Conductivity				Dielectric Properties		Reference
	σ (S cm^{-1})	E_a (eV)	T (K)	RH (%)	ε'	f (Hz)	
Sm-fum-7H_2O	4.69×10^{-4}	0.12	298	97	2.22×10^3	$10^{2.5}$	This work
Er-fum-12H_2O	5.66×10^{-5}	0.27	298	97	1.42×10^5	$10^{2.5}$	This work
$[C_4H_{12}N_2][Ag_4(hedp)_2]$ [a]	1.3×10^{-6}	1.23	298	-	1.6×10^4	2.5×10^5	58
$[C_4H_{12}N_2][Ag_{10}(hedp)_4(H_2O)_2]\cdot 2H_2O$	1.4×10^{-5}	1.18	298	-	2.1×10^4	2.5×10^2	58
$[Ag(C_{10}H_8N_2)(H_4hedp)]$	-	-	-	-	157	10^3	59
$[Ag_2(C_{10}H_8N_2)(H_3hedp)]\cdot 2H_2O$	-	-	-	-	191	10^3	59
$[C_4H_{12}N_2][Ag_4(H_2hedp)_2]$	-	-	-	-	3408	10^3	59
$[C_4H_{12}N_2][Ag_{10}(H_2hedp)_4(H_2O)_2]\cdot 2H_2O$	-	-	-	-	5990	10^3	59
$[Ni(Hci)_2(NH_3)_4]$[b]	6.22×10^{-4}	0.252	298	97	26	10^2	60
$[Ni(Hci)_2(H_2O)_4]$	5.44×10^{-5}	0.298	298	97	38	10^2	60
JUC-125[c]	6.3×10^{-5}	0.32	298	97	80	10^2	41
OCC 1[d]	8.39×10^{-5}	0.41	298	97	156	10^2	43
OCC 2[e]	2.88×10^{-4}	0.21	298	97	2480	10^2	43
$\{[Mg(4,4'\text{-bpdc})(H_2O)_3](H_2O)\}_n$[f]	1.44×10^{-5}	0.277	308	-	200	1500	61
LiTFTA[g]	1.10×10^{-6}	0.56	298	-	50	-	62

Note: σ = proton conductivity (S cm^{-1}), E_a = activation energy (eV), T = temperature (K), RH = relative humidity (%), ε' = dielectric permittivity, f = frequency (Hz). [a] H_5hedp = 1-hydroxyethane-1,1-diphosphonic acid. [b] H_2Ci = 1H-indazole-5-carboxylic acid. [c] JUC-125 = $\{[Gd_4(R\text{-ttpc})_2(R\text{-}Httpc)_2(HCOO)_2(H_2O)_8]\cdot 4H_2O\}_n$, R-$H_3$ttpc = (3R, 3′R, 3″R)-1,1′,1″-(1,3,5-triazine-2,4,6-triyl)-tripiperidine-3-carboxylic acid. [d] OCC 1 = $[(H_3betc)(H\text{-}Hopip)_{0.5}(H_2O)]$, H_4betc = 1,2,4,5-benzenetetracarboxylic acid, Hopip = homopiperazine. [e] OCC 2 = $(H_3betc)_2(H_2\text{-}Mepip)\cdot(H_2O)$, Mepip = 2-methylpiperazine. [f] 4,4′-bpdc = 4,4′-biphenyl dicarboxylate. [g] LiTFTA = lithium tetrahydrofuran-2,3,4,5-tetracarboxylate.

XIX. References for electronic supplementary information

1 W. H. Zhu, Z. M. Wang and S. Gao, A 3D porous lanthanide–fumarate framework with water hexamer occupied cavities, exhibiting a reversible dehydration and rehydration procedure, *Dalton Trans.*, 2006, **6**, 765–768.

2 A. Michaelides, S. Skoulika, E. G. Bakalbassis and J. Mrozinski, Cyclic water hexamers and decamers in a porous lanthanide–organic framework: correlation between some physical properties and crystal structure, *Cryst. Growth Des.*, 2003, **3**, 487–492.

3 J. M. Taylor, S. Dekura, R. Ikeda and H. Kitagawa, Defect control to enhance proton conductivity in a metal–organic framework, *Chem. Mater.*, 2015, **27**, 2286–2289.

4 H. Wang, T. Wen, Z. Shao, Y. Zhao, Y. Cui, K. Gao, W. Xu and H. Hou, High proton conductivity in Nafion/Ni–MOF composite membranes promoted by ligand exchange under ambient conditions, *Inorg. Chem.*, 2021, **60**, 10492–10501.

5 Y.-W. Bai, G. Shi, J. Gao and F. N. Shi, MOF decomposed for the preparation of Co_3O_4/N–doped carbon with excellent microwave absorption, *J. Solid State Chem.*, 2020, **288**, 121401.

6 X. Fan, A. Zhang, M. Li, H. Xu, J. Xue, F. Ye and L. Cheng, A reduced graphene oxide/bi–MOF–derived carbon composite as high–performance microwave absorber with tunable dielectric properties, *J. Mater. Sci.: Mater. Electron.* , 2020, **31**, 11774–11783.

7 X. Xie, Z. Zhang, J. Zhang, L. Hou, Z. Li and G. Li, Impressive proton conductivities of two highly stable metal–organic frameworks constructed by substituted imidazoledicarboxylates, *Inorg. Chem.*, 2019, **58**, 5173–5182.

8 Y. Tian, G. Liang, T. Fan, J. Shang, S. Shang, Y. Ma, R. Matsuda, M. Liu, M. Wang, L. Li and S. Kitagawa, Grafting free carboxylic acid groups onto the pore surface of 3D porous coordination polymers for high proton conductivity, *Chem. Mater.*, 2019, **31**, 8494–8503.

9 J. Wang, Y. Li, M. Jiang, Y. Liu, L. Zhang and P. Wu, A highly chemically stable metal–organic framework as a luminescent probe for the regenerable ratiometric sensing of pH, *Chem. Eur. J.*, 2016, **22**, 13023–13027.

10 F. F. Li, W. R. Cui, W. Jiang, C. R. Zhang, R. P. Liang and J. D. Qiu, Stable sp carbon-conjugated covalent organic framework for detection and efficient adsorption of uranium from radioactive wastewater, *J. Hazard. Mater.*, 2020, **392**, 122333.

11 Y. Chen, B. Wang, X. Wang, L. H. Xie, J. Li, Y. Xie and J. R. Li, A copper(II)-paddlewheel metal–organic framework with exceptional hydrolytic stability and selective adsorption and detection ability of aniline in water, *ACS Appl. Mater. Interfaces*, 2017, **9**, 27027–27035.

12 S. Rodríguez-Hermida, M. Y. Tsang, C. Vignatti, K. C. Stylianou, V. Guillerm, J. Pérez-Carvajal, F. Teixidor, C. Viñas, D. Choquesillo-Lazarte, C. Verdugo-Escamilla, I. Peral, J. Juanhuix, A. Verdaguer, I. Imaz, D. Maspoch and J. Giner Planas, Switchable surface hydrophobicity–hydrophilicity of a metal–

organic framework, *Angew. Chem. Int. Ed.*, 2016, **55**, 16049–16053.
13 K. Wang, D. Feng, T. F. Liu, J. Su, S. Yuan, Y. P. Chen, M. Bosch, X. Zou and H. C. Zhou, A series of highly stable mesoporous metalloporphyrin Fe-MOFs, *J. Am. Chem. Soc.*, 2014, **136**, 13983–13986.
14 D. Feng, K. Wang, Z. Wei, Y. P. Chen, C. M. Simon, R. K. Arvapally, R. L. Martin, M. Bosch, T. F. Liu, S. Fordham, D. Yuan, M. A. Omary, M. Haranczyk, B. Smit and H. C. Zhou, Kinetically tuned dimensional augmentation as a versatile synthetic route towards robust metal–organic frameworks, *Nat. Commun.*, 2014, **5**, 5723.
15 D. Feng, K. Wang, J. Su, T. F. Liu, J. Park, Z. Wei, M. Bosch, A. Yakovenko, X. Zou and H. C. Zhou, A highly stable zeotype mesoporous zirconium metal–organic framework with ultralarge pores, *Angew. Chem. Int. Ed.*, 2014, **54**, 149–154.
16 Y. J. Yang, Y. H. Li, D. Liu and G. H. Cui, A dual-responsive luminescent sensor based on a water-stable Cd(ii)-MOF for the highly selective and sensitive detection of acetylacetone and $Cr_2O_7^{2-}$ in aqueous solutions, *CrystEngComm*, 2020, **22**, 1166–1175.
17 Y. Yang, L. Chen, F. Jiang, M. Wu, J. Pang, X. Wan and M. Hong, A water-stable 3D Eu-MOF based on a metallacyclodimeric secondary building unit for sensitive fluorescent detection of acetone molecules, *CrystEngComm*, 2019, **21**, 321–328.
18 W. J. Phang, W. R. Lee, K. Yoo, D. W. Ryu, B. Kim and C. S. Hong, pH-dependent proton conducting behavior in a metal–organic framework material, *Angew. Chem.*, 2014, **126**, 8523–8527.
19 X. Liang, S. Wang, S. Zhang, C. Lin, F. Xie, R. Li, F. Zhang, C. Wen, L. Feng and C. Wan, High proton conductivity modulated by active protons in 1D ultra-stable metal–organic coordination polymers: a new insight into the coordination interaction/ability of metal ions, *Inorg. Chem. Front.*, 2023, **10**, 1238–1254.
20 S. Wang, F. Xie, S. Zhang, X. Liang, Q. Gao, Y. Chen, F. Zhang, C. Wen, L. Feng and C. Wan, Water-assisted proton conduction regulated by hydrophilic groups in metallo-hydrogen-bonded organic frameworks: “like-attracts-like” between hydrophilic groups and water molecules, *CrystEngComm*, 2023, **25**, 4701–4715.
21 F. Costantino, A. Donnadio and M. Casciola, Survey on the phase transitions and their effect on the ion-exchange and on the proton-conduction properties of a flexible and robust Zr phosphonate coordination polymer, *Inorg. Chem.*, 2012, **51**, 6992–7000.
22 S. Biswas, J. Chakraborty, V. Singh Parmar, S. P. Bera, N. Ganguli and S. Konar, Channel-assisted proton conduction behavior in hydroxyl-rich Lanthanide-based magnetic metal–organic frameworks, *Inorg. Chem.*, 2017, 56, 4956–4965.
23 X. Meng, H. N. Wang, L. S. Wang, Y. H. Zou and Z. Y. Zhou, Enhanced proton conductivity of a MOF-808 framework through anchoring organic acids to the zirconium clusters by post-synthetic modification, *CrystEngComm*, 2019, **21**, 3146–3150.
24 X. Y. Dong, X. P. Hu, H. C. Yao, S. Q. Zang, H. W. Hou and T. C. W. Mak, Alkaline earth metal (Mg, Sr, Ba)–organic frameworks based on 2,2′,6,6′-tetracarboxybiphenyl for proton conduction, *Inorg. Chem.*, 2014, **53**, 12050–

12057.
25 F. M. Zhang, L. Z. Dong, J. S. Qin, W. Guan, J. Liu, S. L. Li, M. Lu, Y. Q. Lan, Z. M. Su and H. C. Zhou, Effect of imidazole arrangements on proton-conductivity in metal–organic frameworks, *J. Am. Chem. Soc.*, 2017, **139**, 6183–6189.
26 W. Chen, C. Yang, S. Yu, Z. Li and G. Li, Proton conduction and impedance sensing of a highly stable copper–organic framework from imidazole dicarboxylate, *Polyhedron*, 2019, **158**, 377–385.
27 X. Xie, Z. Zhang, J. Zhang, L. Hou, Z. Li and G. Li, Impressive proton conductivities of two highly stable metal–organic frameworks constructed by substituted imidazoledicarboxylates, *Inorg. Chem.*, 2019, **58**, 5173–5182.
28 M. Wei, X. Wang and X. Duan, Crystal structures and proton conductivities of a MOF and two POM–MOF composites based on Cu^{II} ions and 2,2′-bipyridyl-3,3′-dicarboxylic acid, *Chem. Eur. J.*, 2012, **19**, 1607–1616.
29 S. K. Konavarapu, A. Goswami, A. G. Kumar, S. Banerjee and K. Biradha, MOFs containing a linear bis-pyridyl-tris-amide and angular carboxylates: exploration of proton conductivity, water vapor and dye sorptions, *Inorg. Chem. Front.*, 2019, **6**, 184–191.
30 R. Liu, L. Zhao, S. Yu, X. Liang, Z. Li and G. Li, Enhancing proton conductivity of a 3D metal–organic framework by attaching guest NH_3 molecules, *Inorg. Chem.*, 2018, **57**, 11560–11568.
31 X. M. Li, J. Liu, C. Zhao, J. L. Zhou, L. Zhao, S. L. Li and Y. Q. Lan, Strategic hierarchical improvement of superprotonic conductivity in a stable metal–organic framework system, *J. Mater. Chem. A*, 2019, **7**, 25165–25171.
32 X. Liang, B. Li, M. Wang, J. Wang, R. Liu and G. Li, Effective approach to promoting the proton conductivity of metal–organic frameworks by exposure to aqua–ammonia vapor, *ACS Appl. Mater. Interfaces*, 2017, **9**, 25082–25086.
33 W. Chen, L. Zhao, S. Yu, Z. Li, J. Feng and G. Li, Two water-stable 3D supramolecules supported by hydrogen bonds for proton conduction, *Polyhedron*, 2018, **148**, 100–108.
34 Y. Y. Yuan, S. L. Yang, C. X. Zhang and Q. L. Wang, A new europium metal–organic framework with both high proton conductivity and highly sensitive detection of ascorbic acid, *CrystEngComm*, 2018, **20**, 6989–6994.
35 M. Y. Xu, Y. L. Wang, Q. Liu, Z. T. Lin and Q. Y. Liu, Lanthanide 5,7-disulfonate-1,4-naphthalenedicarboxylate frameworks constructed from trinuclear and tetranuclear Lanthanide carboxylate clusters: proton conduction and selective fluorescent sensing of Fe^{3+}, *Inorg. Chem.*, 2020, **59**, 7265–7273.
36 X. Y. Dong, R. Wang, J. Z. Wang, S. Q. Zang and T. C. W. Mak, Highly selective Fe^{3+} sensing and proton conduction in a water-stable sulfonate–carboxylate Tb–organic-framework, *J. Mater. Chem. A*, 2015, **3**, 641–647.
37 M. J. Wei, J. Q. Fu, Y. D. Wang, Y. Zhang, H. Y. Zang, K. Z. Shao, Y. G. Li and Z. M. Su, Highly tuneable proton-conducting coordination polymers derived from a sulfonate-based ligand, *CrystEngComm*, 2017, **19**, 7050–7056.
38 J. Lee, D. W. Lim, S. Dekura, H. Kitagawa and W. Choe, MOP × MOF: collaborative combination of metal–organic polyhedra and metal–organic

framework for proton conductivity, *ACS Appl. Mater. Interfaces*, 2019, **11**, 12639–12646.

39 X. Liang, and Z. Fan, Structural characterization and proton-conductive property of a lanthanide metal-organic framework assembled from 1, 2, 4, 5-benzenetetracarboxylic acid and piperazine, *Chin. J. Struct. Chem.*, 2017, **36**, 977–984.

40 X. Liang, T. Cao, L. Wang, C. Zheng, Y. Zhao, F. Zhang, C. Wen, L. Feng and C. Wan, From an organic ligand to a metal–organic coordination polymer, and to a metal–organic coordination polymer–cocrystal composite: a continuous promotion of the proton conductivity of crystalline materials, *CrystEngComm*, 2020, **22**, 1414–1424.

41 X. Liang, F. Zhang, H. Zhao, W. Ye, L. Long and G. Zhu, A proton-conducting lanthanide metal–organic framework integrated with a dielectric anomaly and second-order nonlinear optical effect, *Chem. Commun.*, 2014, **50**, 6513–6516.

42 X. Liang,R. Li and Z. Fan, Hydrothermal synthesis, crystal structure and proton conductivity of a Pr–Ca heterometal-organic framework generated by 1, 2, 4, 5-benzenetetracarboxylic acid, *Chin. J. Struct. Chem.*, 2017, **36**, 993–1002.

43 X. Liang, Y. Chen, L. Wang, F. Zhang, Z. Fan, T. Cao, Y. Cao, H. Zhu, X. He, B. Deng, Y. You, Y. Dong and Y. Zhao, Effect of carbon-skeleton isomerism on the dielectric properties and proton conduction of organic cocrystal compounds assembled from 1,2,4,5-benzenetetracarboxylic acid and piperazine derivatives, *New J. Chem.*, 2019, **43**, 11099–11112.

44 X. Liang, K. Cai, F. Zhang, J. Liu and G. Zhu, A proton-conductive lanthanide oxalatophosphonate framework featuring unique chemical stability: stabilities of bulk phase and surface structure, *J. Mater. Chem. A*, 2017, **5**, 25350–25358.

45 X. Liang, K. Cai, F. Zhang, J. Liu and G. Zhu, One, two, and three-dimensional metal–organic coordination polymers derived from enantiopure organic phosphorate: homochirality, water stability and proton conduction, *CrystEngComm*, 2017, **19**, 6325–6332.

46 B. Huang, S. Zhang, C. Wan, X. Liang, F. Zhang, L. Feng and C. Wen, Combined Effect of Hydrophilic Pore and the Type of Protons on Proton Conductivity in Porous Metal–Organic Frameworks: A Feasible Approach to Achieve a Super Proton Conductor under Hydrated Conditions, Inorganic Chemistry, 2024, 63, 16688-16701.

47 D. W. Fu, H. Y. Ye, Q. Ye, K. J. Pan and R. G. Xiong, Ferroelectric metal–organic coordination polymer with a high dielectric constant, *Dalton Trans.*, 2008, **7**, 874–877.

48 A. Pathak, G. R. Chiou, N. R. Gade, M. Usman, S. Mendiratta, T. T. Luo, T. W. Tseng, J. W. Chen, F. R. Chen and K. H. Chen, High-κ samarium-based metal–organic framework for gate dielectric applications, *ACS Appl. Mater. Interfaces*, 2017, **9**, 21872–21878.

49 M. Guo, H. L. Cai and R. G. Xiong, Ferroelectric metal organic framework (MOF), *Inorg. Chem. Commun.*, 2010, **13**, 1590–1598.

50 M. Sánchez-Andújar, S. Yáñez-Vilar, B. Pato-Doldán, C. Gómez-Aguirre, S.

Castro-García and M. A. Señarís-Rodríguez, Apparent colossal dielectric constants in nanoporous metal organic frameworks, *J. Phys. Chem. C*, 2012, **116**, 13026–13032.

51 S. Kamal, K. R. Chiou, B. Sainbileg, A. I. Inamdar, M. Usman, A. Pathak, T. T. Luo, J. W. Chen, M. Hayashi, C. H. Hung and K. L. Lu, Thermally stable indium based metal–organic frameworks with high dielectric permittivity, *J. Mater. Chem. C*, 2020, **8**, 9724–9733.

52 X. Peng, W. Xu, L. Chen, Y. Ding, S. Chen, X. Wang and H. Hou, Polyimide complexes with high dielectric performance: toward polymer film capacitor applications, *J. Mater. Chem. C*, 2016, **4**, 6452–6456.

53 W. J. Ji, Q. G. Zhai, S. N. Li, Y. C. Jiang and M. C. Hu, The first ionothermal synthesis of a 3D ferroelectric metal–organic framework with colossal dielectric constant, *Chem. Commun.*, 2011, **47,** 3834–3836.

54 C. C. Homes, T. Vogt, S. M. Shapiro, S. Wakimoto and A. P. Ramirez, Optical response of high-dielectric-constant perovskite-related oxide, *Science*, 2001, **293**, 673–676.

55 Q. Ye, Y. M. Song, G. X. Wang, K. Chen, D. W. Fu, P. W. Hong Chan, J. S. Zhu, S. D. Huang and R. G. Xiong, Ferroelectric metal− organic framework with a high dielectric constant, *J. Am. Chem. Soc.*, 2006, **128**, 6554–6555.

56 H. He, Y. Cui, B. Li, B. Wang, C. Jin, J. Yu, L. Yao, Y. Yang, B. Chen and G. Qian, Confinement of perovskite-QDs within a single MOF crystal for significantly enhanced multiphoton excited luminescence, *Adv. Mater.*, 2018, **31**, 1806897.

57 S. Laha, A. Chakraborty and T. K. Maji, Synergistic role of microwave and perturbation toward synthesis of hierarchical porous MOFs with tunable porosity, *Inorg. Chem.*, 2020, **59**, 3775–3782.

58 T. Rom, N. Kumar, M. Sharma, A. Gaur and A. K. Paul, Colossal dielectric responses from the wide band gap 2D-semiconducting amine templated hybrid framework materials, *Inorg. Chem.*, 2020, **59**, 9465–9470.

59 T. Rom and A. K. Paul, Role of aromatic vs. aliphatic amine for the variation of structural, electrical and catalytic behaviors in a series of silver phosphonate extended hybrid solids, *Dalton Trans.*, 2020, **49**, 13618–13634.

60 S. Feng, F. Xie, C. Wan, F. Zhang, L. Feng, C. Wen and X. Liang, Impact of the number of hydrogen bonds on proton conductivity in metallo–hydrogen–bonded organic frameworks: the more the number of hydrogen bonds, the better the proton conductivity at the maximum relative humidity, *CrystEngComm*, 2024, **26**, 4855–4870.

61 S. Singha, S. K. Maity, S. Biswas, R. Saha and S. Kumar, A magnesium-based bifunctional MOF: studies on proton conductivity, gas and water adsorption, *Inorg. Chim. Acta*, 2016, **453**, 321–329.

62 V. Zima, K. Shimakawa and C. H. Lin, Protonic conductivity of polycrystalline materials evaluated with effective medium percolation approach: A case study on lithium-carboxylate based MOF, *Solid State Ionics*, 2016, **292**, 98–102.